Title

Extraordinary Redox Activities in Ladder-Type Conjugated Molecules Enabled by B ← N Coordination-Promoted Delocalization and Hyperconjugation

Journal

Journal of the American Chemical Society, 140(51)

ISSN

0002-7863

Authors

Zhu, Congzhi

Ji, Xiaozhou

You, Di

et al.

Publication Date

2018-12-26

DOI

10.1021/jacs.8b11337

Peer reviewed

JACS
JOURNAL OF THE AMERICAN CHEMICAL SOCIETY

Article

pubs.acs.org/JACS

Extraordinary Redox Activities in Ladder-Type Conjugated Molecules Produced by B ← N Coordination-Promoted Delocalization and Hyperconjugation

Congzhi Zhu,[†] Xiaozhou Ji,[†] Di You,[†] Teresa L. Chen,[§] Anthony U. Mu,[†] Kayla P. Barker,[†] Liana M. Klivansky,[§] Yi Liu,[§] and Lei Fang*[,†,‡]

[†]Department of Chemistry and [‡]Department of Materials Science and Engineering, Texas A&M University, 3255 TAMU, College Station, Texas 77843, United States

[§]The Molecular Foundry, Lawrence Berkeley National Laboratory, One Cyclotron Road, Berkeley, California 94720, United States

Supporting Information

ABSTRACT: The introduction of B ← N coordination—isoelectronic to C−C single bond—into π-systems represents a promising strategy to impart exotic redox and electrochromic properties into conjugated organic molecules and macromolecules. To achieve both reductive and oxidative activities using this strategy, a cruciform ladder-type molecular constitution was designed to accommodate oxidation-active, reduction-active, and B ← N coordination units into a compact structure. Two such compounds (**BN-F** and **BN-Ph**) were synthesized via highly efficient N-directed borylation. These molecules demonstrated well-separated, two-reductive and two-oxidative electron-transfer processes, corresponding to five distinct yet stable oxidation states, including a rarely observed boron-containing radical cation. Spectroelectrochemical measurements revealed unique optical characteristics for each of these reduced/oxidized species, demonstrating multicolor electrochromism with excellent recyclability. Distinct color changes were observed between each redox state with clear isosbestic points on the absorption spectra. The underlying redox mechanism was elucidated by a combination of computational and experimental investigations. Single-crystal X-ray diffraction analysis on the neutral state, the oxidized radical cation, and the reduced dianion of **BN-Ph** revealed structural transformations into two distinct quinonoid constitutions during the oxidation and reduction processes, respectively. B ← N coordination played an important role in rendering the robust and reversible multistage redox properties, by extending the charge and spin delocalization, by modulating the π-electron density, and by a newly established hyperconjugation mechanism.

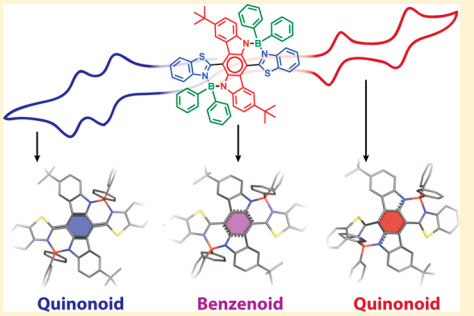

INTRODUCTION

Ladder-type conjugated molecules, constituted with an uninterrupted sequence of fused adjacent rings that share two or more atoms with one another, have shown great promise for applications on multiple fronts that demand superior optical, electronic, or mechanical properties.[1−10] Stemming from the strong intramolecular electronic couplings throughout fused conjugated backbones, ladder-type conjugated compounds also demonstrate intriguing electrochemical behaviors, such as the capability of undergoing multiple electron transfers.[7,11] The extended conjugation and rigid backbones can greatly stabilize the highly reactive radical and ionic intermediates that are generated during the redox processes. For instance, ladder-type oligothiophene exhibited stepwise oxidations.[7,12] A recently reported series of ladder-type conjugated polycyclic hydrocarbons, featuring extensive graphitic constitutions, demonstrated four distinct reversible redox processes.[13] In this context, ladder-type molecular design represents an important strategy to achieve exotic molecular materials desirable for sophisticated electrochemical applications.[11,14,15]

To date, redox-active ladder-type compounds are mostly fused with entirely covalent bonds.[1,3,4] Alternatively, intramolecular noncovalent B ← N coordination[16−19] has been exploited to serve as a bridge to construct ladder-type conjugated molecules while imparting modification to the aromatic character.[20,21] Compared to the isoelectronic and isosteric C−C single bond, intramolecular B ← N coordination in a conjugated molecule not only extends the π-delocalization but also dramatically changes the electronic structures, electronic and optical properties,[17−19,22−32] and reactivities,[33,34] because of the intrinsically different valence electron configurations and electronegativities of boron and nitrogen compared to carbon. For instance, the incorporation of B ← N coordination into conjugated molecules deepens the lowest unoccupied molecular orbital (LUMO) energy levels, which facilitate reductive electron-transfer processes.[17,19,25−27,35] Additionally, boron atoms can couple with a neighboring unpaired spin, providing additional stabilization effects for

Received: October 21, 2018
Published: December 3, 2018

DOI: 10.1021/jacs.8b11337
J. Am. Chem. Soc. XXXX, XXX, XXX−XXX

radical intermediates during redox processes.[35−38] Therefore, the employment of B ← N coordination represents a powerful strategy to develop novel conjugated molecules and macromolecules with new redox properties that were not accessible before.

Despite the great potential of this noncovalent approach, however, it is still challenging to achieve robust redox activities in B ← N bridged ladder-type molecules, especially oxidation processes, because of the electron-deficient nature of boron moieties and the resulting low stability of the corresponding oxidized states. Meanwhile, the underlying mechanism of the redox processes of B ← N bridged ladder-type molecules remains unclear, especially on the impacts of tetracoordinated boron centers on the electronic structures and optical characteristics of these molecules. Herein, we report a molecular design strategy that allowed for the access to five redox states, both reduced and oxidized, of B ← N bridged ladder-type molecules, as well as the corresponding mechanistic investigations.

RESULTS AND DISCUSSION

To pursue both robust reductive and oxidative electron-transfer processes in B ← N bridged ladder-type molecules, we envisioned that the molecular design should first integrate multiple redox-active components in an orthogonal and compact manner, so that multiple electron-transfer processes can be enabled in a small molecule without interfering with each other. Second, B ← N coordination needs to be installed to rigidify the π-system to facilitate the desired delocalization of charges and spins, therefore stabilizing the reduced or oxidized species. On the basis of these principles, we designed a ladder-type molecule composed of an oxidation-active indolo[3,2-*b*]carbazole (ICBZ) unit and two reduction-active benzo[*d*]thiazole (BTH) units (Figure 1a). The ICBZ unit is

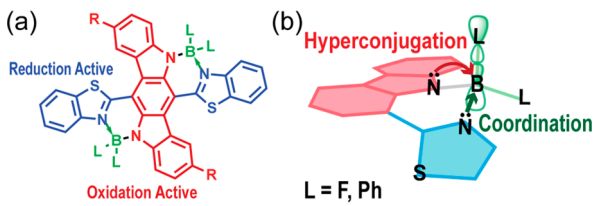

Figure 1. (a) Designed ladder-type molecule featuring cruciform arrangement of redox-active units (reduction-active in blue and oxidation-active in red) and B ← N coordination that can rigidify and coplanarize the entire molecule; (b) representative orbital interactions of the boron center in the designed conjugated backbone.

covalently linked to the BTH units at the 6 and 12 positions, leading to a cruciform-like geometry, generating two distinctive delocalization regions for oxidation and reduction, respectively. On one hand, ICBZ is known to undergo two-electron oxidation processes into a relatively stable quinonoid structure.[39,40] The two N−H functionalities on ICBZ provided the point to covalently attach the boron centers.[41−43] Indeed, B ← N bridged ladder-type ICBZ derivatives reported by Curiel et al.[43] showed the expected reversible electrochemical oxidation behavior. In our design, tertiary butyl groups are installed at the 2 and 8 positions of ICBZ to ensure the solubility of this rigid compound. On the other hand, BTH was selected as the reduction-active unit.[44] The Lewis basic nitrogen atoms on the thiazole rings were employed to form the B ← N coordination.

The B ← N coordination in this molecular design was formed in a geometrically favored six-membered heterocycle architecture, which fused the ICBZ and BTH units into a ladder-type structure. The N−B ← N constitution was expected to be stable not only in ambient condition but also during redox processes, similar to the known stability of BODIPY dyes.[45,46] The strong B ← N coordination significantly withdrew the electron density from BTH units, resulting in an enhanced electron affinity.[17,19,25] Consequently, the reduction of such a molecule could fall into an accessible potential range. Moreover, this boron-containing six-membered heterocycle architecture reassembles the structure of cyclohexa-1,3-diene, in which a series of hyperconjugative interactions were previously observed to significantly impact the molecular conformation, properties, and stability.[47,48] In this design, the sp^3 hybridized boron atom carried two ligands that were expected to undergo hyperconjugative interactions similar to those existing in cyclohexa-1,3-diene (Figure 1b). We hypothesized that these hyperconjugative interactions could further stabilize the radical intermediates upon reduction/oxidation, by assisting the charge and spin delocalization. Consequently, the low-energy singly occupied molecular orbital (SOMO) to LUMO transition of these stabilized organic radicals could be utilized to achieve electrochromism in the near-infrared (NIR) region,[49] which is highly desired for various applications including data storage, smart windows, and sensing.[11,50−52]

On the basis of this design principle, two molecular candidates, **BN-F** and **BN-Ph**, with fluoride and phenyl groups attached to the boron center as ligands, respectively, were synthesized. The syntheses were accomplished (Scheme 1) in

Scheme 1. Synthesis of BN-F and BN-Ph

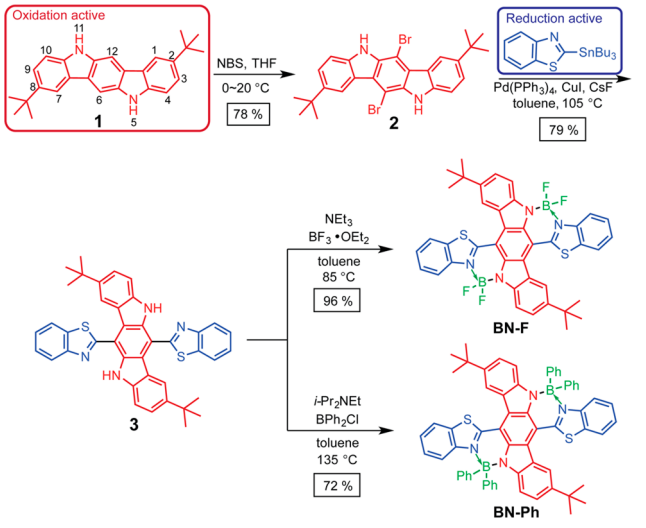

three steps starting from 2,8-di-*tert*-butyl-5,11-dihydroindolo-[3,2-*b*]carbazole (compound **1**). First of all, treatment of **1** with 2.0 equiv of *N*-bromosuccinimide (NBS) selectively brominated the 6- and 12-positions to give a dibromo derivative, **2**. Compound **2** was subsequently subjected to Stille coupling reaction with 2-(tributylstannyl)benzo[*d*]-thiazole. CuI and CsF were used to facilitate the transmetalation step[53] during the Stille reaction to give intermediate **3**. In this step, temperature control was crucial to achieve a high yield. Significant side reactions were found above 130 °C,

DOI: 10.1021/jacs.8b11337
J. Am. Chem. Soc. XXXX, XXX, XXX−XXX

which was likely a result of undesired copper-catalyzed reactions, such as Ullmann coupling.[54] Finally, borylation of **3** with BF_3 and BPh_2Cl in the presence of non-nucleophilic bases afforded the desired products in excellent isolated yields (96% and 72%, respectively). Notably, the isolation yield of **BN-Ph** was significantly improved compared to a previously reported reaction using BPh_3 to introduce B ← N coordinate bonds into a similar ICBZ backbone,[43] likely due to the higher electrophilicity and smaller steric hindrance of BPh_2Cl. **BN-F** and **BN-Ph** showed good stabilities in ambient conditions. For example, **BN-Ph** was purified by normal-phase silica gel chromatography. Both final products were fully characterized by NMR spectroscopy and mass spectrometry. In addition, **BN-Ph** was characterized unambiguously by single-crystal X-ray diffraction analysis. Single crystals of **BN-Ph** suitable for X-ray diffraction analysis were obtained by vapor diffusion of pentane into a chloroform solution. Tetrahedral geometry of the boron centers was revealed, with a short B ← N coordinate bond length of 1.643 Å. The anticipated rigid conformation of **BN-Ph** bridged by the B ← N coordination was validated in the solid-state crystal structure. The dihedral angles between ICBZ units and BTH units were measured to be 20.0° in **BN-Ph**, significantly smaller than that observed in the density functional theory (DFT) computed, energy-minimized geometry of the precursor **3** (Figure S12).

DFT calculations on the π-conjugated backbone revealed extended π-delocalization on **BN-F** and **BN-Ph**. The visualized highest occupied molecular orbitals (HOMOs) of both molecules were delocalized over the entire conjugated backbones with non-negligible contributions from the boron centers and the ligands (Figure S11). The majority of LUMOs were on the electron-deficient BTH units and the boron centers. Time-dependent DFT calculations afforded multiple optical transitions with significant intensities, including the lowest band gap HOMO → LUMO transitions, and the higher-energy HOMO−1 → LUMO transitions. These transitions matched well with experimental spectra. Both **BN-F** and **BN-Ph** possessed low band gap NIR absorptions and fluorescent emissions. For example, the UV−vis−NIR spectrum of a dilute solution of **BN-F** in CH_2Cl_2 showed the low-energy HOMO → LUMO absorption peak at 695 nm (ε = 1.17×10^4 $M^{-1}\cdot cm^{-1}$) (Figure 2a). For **BN-Ph** with phenyl ligands on the boron center, such HOMO → LUMO band red-shifted into the NIR region (λ_{max} = 768 nm, $\varepsilon = 1.80 \times 10^4$ $M^{-1}\cdot cm^{-1}$) (Figure 2b). The presence of vibrational progression in both spectra indicated the rigid nature of **BN-F** and **BN-Ph**.[1,2] Fluorescence emission of **BN-F** and **BN-Ph** appeared in the NIR region with λ_{max} at 720 and 812 nm in CH_2Cl_2, respectively (Figure 2a and b). Small Stokes shifts (576 cm^{-1} for **BN-F** and 705 cm^{-1} for **BN-Ph**) also implied their backbone rigidity, due to the lack of energy loss associated with conformational changes during the excitation−emission processes. The fluorescence quantum yields of **BN-F** and **BN-Ph** were measured using reference standards (zinc phthalocyanine for **BN-F** and indocyanine green for **BN-Ph**) to be 2.8% and 1.2% in CH_2Cl_2, respectively.

On the basis of the molecular design, **BN-F** and **BN-Ph** were expected to undergo multistage electron-transfer processes. Indeed, cyclic voltammograms (CVs) unveiled four well-separated, reversible electron-transfer processes in both **BN-F** and **BN-Ph** (Figure 3), indicating five accessible redox states for both compounds. The excellent reversibility of these processes indicated the high stability of all the states including

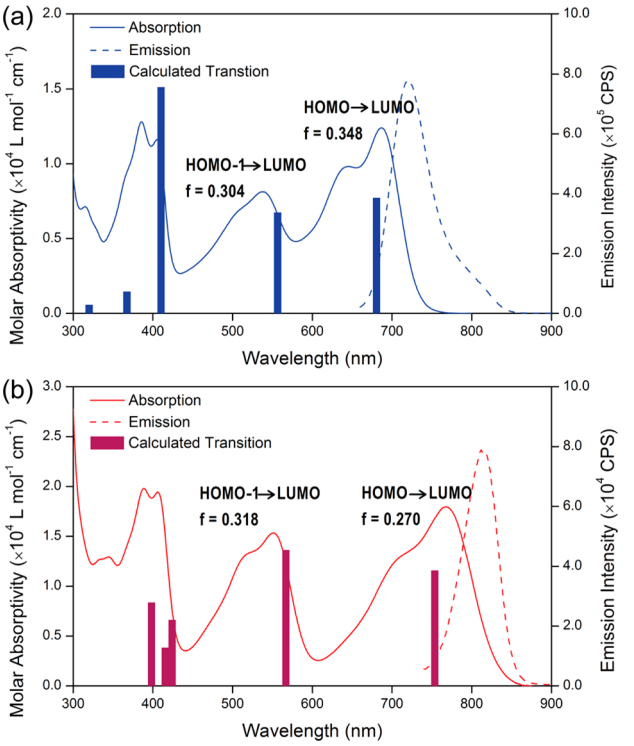

Figure 2. UV−vis−NIR absorption (solid lines) and emission (dashed lines) of (a) **BN-F** and (b) **BN-Ph** in CH_2Cl_2 with transition energies calculated by time-dependent DFT (TD-DFT) using B3LYP/6-311g(d,p) with CH_2Cl_2 CPCM solvation.

radical anions (−1), dianions (−2), radical cations (+1), and dications (+2). The measured electrochemical band gaps of **BN-F** and **BN-Ph** (1.81 and 1.62 eV, respectively) matched well with the optical band gap (1.78 and 1.60 eV, respectively). Among these two voltammograms, the redox processes of **BN-Ph** appeared cathodically shifted (Figure 3b) compared to that of **BN-F**, likely due to the more electron-rich nature of the phenyl ligand compared to fluoride. Such an effect was more significant on the oxidation processes, leading to a narrower band gap of **BN-Ph** than that of **BN-F**.

All the anodic and cathodic peaks of **BN-F** and **BN-Ph** during both oxidation and reduction sweeps were well-separated, suggesting the good stabilities of the radical anion and radical cation intermediates toward disproportionation. For example, the potential gaps between the two reduction waves for both **BN-F** and **BN-Ph** were ~0.3 V (Figure 3a and b). These values corresponded to large radical comproportionation constants of the reduced forms ($K_{com\text{-}re}$) of 5.41×10^4 for **BN-F** and 1.74×10^5 for **BN-Ph** at 25 °C (equilibrium 1 in Figure 3d), indicating a highly stable radical anion. On the oxidation side, the potential gaps between the two oxidative processes were even larger (0.45 V for **BN-F** and 0.51 V for **BN-Ph**), corresponding to remarkably high radical comproportionation constants ($K_{com\text{-}ox}$) of 4.04×10^7 and 4.17×10^8 at 25 °C, respectively (equilibrium 2 in Figure 3d). Such high stabilities of the radicals were attributed to the strong spin-delocalization on the rigid backbones of **BN-F** and **BN-Ph** as designed. In contrast, precursor **3** without B ← N coordination, as a control, showed overlapping two-electron oxidation processes (Figure 3c) and irreversible reduction processes. Such a drastic difference on the redox behaviors between **BN-F**/**BN-Ph** and **3** demonstrated profound changes

DOI: 10.1021/jacs.8b11337
J. Am. Chem. Soc. XXXX, XXX, XXX−XXX

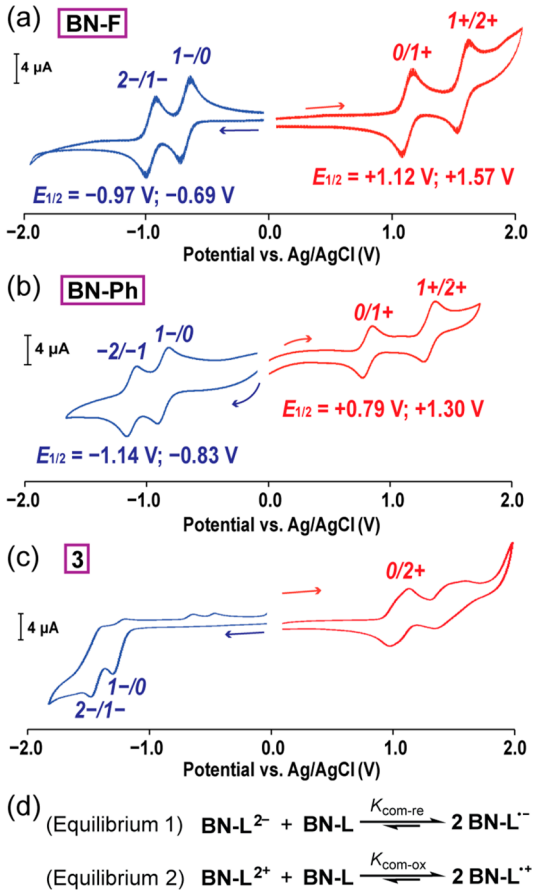

Figure 3. CV curves of (a) **BN-F**, (b) **BN-Ph**, and (c) **3** in CH_2Cl_2 [0.10 M tetrabutylammonium hexafluorophosphate ($TBAPF_6$) as the electrolyte; Ag/AgCl as the reference electrode; scan rate = 100 mV/s]. The half-wave potentials of each redox process were noted in (a) **BN-F** and (b) **BN-Ph**. (d) Comproportionation equilibriums of radical cations and radical anions.

in the electronic structures after the installment of the B ← N coordination. These electrochemical data demonstrated the highly efficient stabilization effect of the B ← N coordination on the oxidized/reduced states through extending charge/spin delocalization.

The excellent redox reversibility allowed spectroelectrochemical measurements on **BN-Ph**, i.e., UV−vis−NIR absorption spectra recorded during each of the electrochemical redox processes, which gave highly reversible multicolor electrochromism (Figure 4a). According to time-dependent DFT calculations, these drastic color changes were attributed to the substantial differences on the transition energy diagrams of the different redox states (Tables S4 and S5). When the applied potential swept from 0.70 to 1.05 V (vs Ag/AgCl), **BN-Ph** was gradually oxidized into the radical cation form **BN-Ph**$^{\bullet+}$. During this process, the HOMO−LUMO transition of the neutral **BN-Ph** at 768 nm diminished, while a new NIR absorption at 1180 nm emerged (Figure 4b). This low-energy absorption band corresponded to the transition of HOMO-β → LUMO-β of the delocalized radical cation (Figure 4d), according to DFT calculation. On the basis of the cutoff shape of this NIR absorption peak, **BN-Ph**$^{\bullet+}$ can be categorized as a class III mixed valence system,[55] in which the two nitrogen-centered redox moieties in ICBZ were strongly coupled with one another. The absorption spectra exhibited no significant change from 1.05 to 1.25 V, indicating the good stability of **BN-Ph**$^{\bullet+}$ over a wide range of potentials. When **BN-Ph**$^{\bullet+}$ was oxidized into the dication form **BN-Ph**$^{2+}$ by increasing the potential from 1.30 to 1.50 V, the characteristic radical cation absorption peak at 1180 nm gradually diminished, while multiple absorption bands covering a broad visible light region emerged (Figure 4c). To test the reversibility of these oxidation processes, iterative potential sweepings were conducted between +0.20, +1.10, and +1.50 V for >15 cycles (Figure 4h). Excellent reversibility was demonstrated without notable degradation of the absorption intensity (monitored at 470 nm).

Similarly, the radical anion and dianion of **BN-Ph** were investigated by spectroelectrochemistry study. Upon the application of a negative potential of −0.75 V, **BN-Ph** started to be reduced as the absorption intensity at 768 nm decreased (Figure 4e) while a highly intensive peak at 677 nm and a weak absorption peak at ∼940 nm emerged, corresponding to the optical transitions, HOMO−1-α → LUMO-α and HOMO-β → LUMO-β of radical anion **BN-Ph**$^{\bullet-}$ (Figure 4g). The Gaussian shape of this low energy peak indicated that **BN-Ph**$^{\bullet-}$ was a class II mixed valence system, in which the two reduced BTH moieties were coupled in a weaker manner.[55,56] Further decrease of the potential from −1.05 to −1.35 V resulted in the second step of reduction into the dianion, **BN-Ph**$^{2-}$, accompanied by the diminishing of all the peaks in the long-wavelength region and the emerging of a higher-energy peak centered at 544 nm as the new HOMO → LUMO transition (Figure 4f). Again, excellent reversibility of the reduction processes was confirmed by monitoring the absorption intensity at 680 nm while sweeping the potential iteratively between −0.30, −1.05, and −1.40 V (Figure 4i) for >15 cycles. Spectroelectrochemical measurements were also conducted in a CH_2Cl_2 solution of **BN-F**, which showed a similar reversible multistage electrochromism over a wide range of electric potentials (Figure S9).

To shed light on the mechanism of these remarkable redox and electrochromic activities of **BN-Ph** and **BN-F**, DFT computations were performed starting with geometry optimization [B3LYP/6-311g(d,p)] for all five redox states of **BN-Ph** in the gas phase. At the neutral state of **BN-Ph**, the lengths of bonds *c*, *d*, and *e* in the central ring "A" (1.412−1.427 Å) were close to that in a benzene ring (Figure 5a). Upon oxidation into the radical cation **BN-Ph**$^{\bullet+}$, DFT calculation showed that the bond length alternation (BLA) between these three bonds increased, indicating a decrease of aromaticity. The BLA increased further in the diradical form **BN-Ph**$^{2+}$ (Figure 5b), so that bonds *c* and *e* were elongated to 1.451 and 1.438 Å, respectively, while bond *d* was shortened to 1.388 Å, close to the bond length of a typical C=C double bond. Additionally, the C=N double bonds *b* and *f* were shortened from 1.366 Å in **BN-Ph** to 1.330 Å in **BN-Ph**$^{2+}$. This computational study revealed a tendency toward quinonoid character of the ICBZ unit after oxidation (Figure 5e). In contrast, optimized geometries of the reduced forms exhibited that a different quinonoid structure was formed in between the two BTH units involving bonds *j*, *k*, *l*, *e*, and *m* (Figure 5c). In this case, bonds *j*, *l*, and *m* were shortened, accompanied by increased lengths of bonds *e* and *k*, during the transformation into **BN-Ph**$^{\bullet-}$ and **BN-Ph**$^{2-}$. These computational results suggested that, in the B ← N bridged molecule, two different yet orthogonal pathways of BLA changes were accessible to two different quinonoid constitutions during the oxidation and

DOI: 10.1021/jacs.8b11337
J. Am. Chem. Soc. XXXX, XXX, XXX−XXX

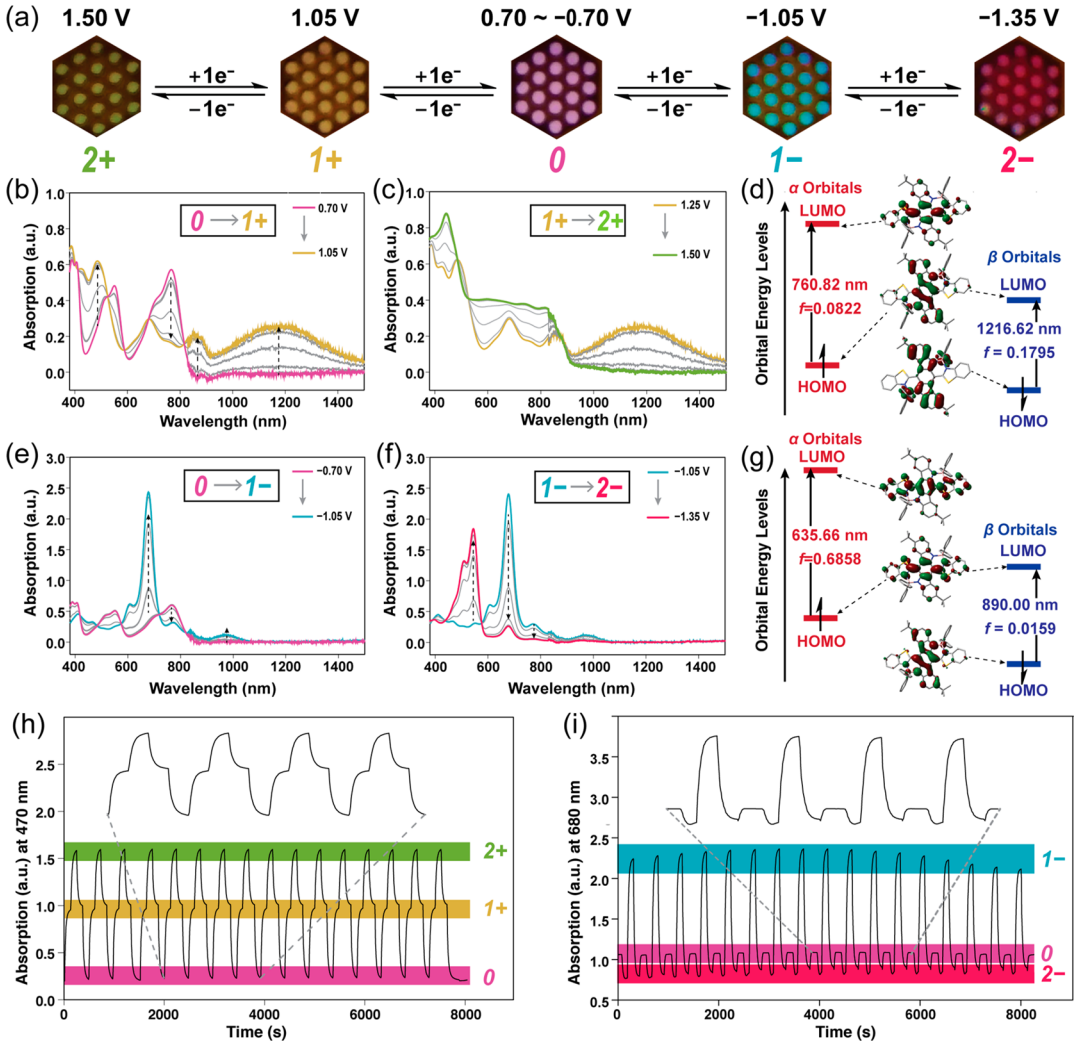

Figure 4. (a) Photographs of the **BN-Ph** solutions at different redox states in the presence of a honeycomb working electrode in a spectroelectrochemical cell (in CH_2Cl_2 with 0.10 M $TBAPF_6$). UV−vis−NIR absorption changes of the **BN-Ph** solutions upon stepwise applications of potentials on the honeycomb working electrode (step height = 0.05 V, vs Ag/AgCl) from (b) +0.70 to +1.05 V, (c) +1.25 to +1.50 V, (e) −0.70 to −1.05 V, and (f) −1.05 to −1.35 V. Molecular frontier orbitals and calculated transition energies of (d) **BN-Ph**$^{\bullet+}$ and (g) **BN-Ph**$^{\bullet-}$ [UB3LYP/6-311g(d,p) with CH_2Cl_2 CPCM solvation]. Multiple cycles of absorption changes of the **BN-Ph** solutions when the potential was switching between (h) 0.20, 1.10, and 1.50 V and (i) −0.30, −1.05, and −1.40 V.

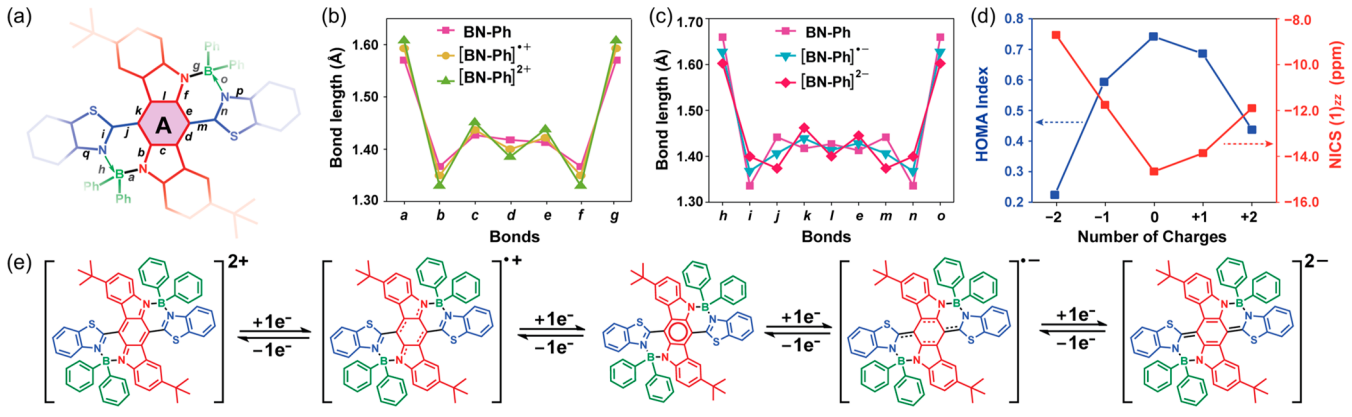

Figure 5. (a) Redox-active core structure of **BN-Ph** labeled with bond indices from *a* to *q*; (b) DFT calculated lengths of the bonds *a*−*g* before and after oxidation; (c) DFT calculated lengths of the bonds *e* and *h*−*o* before and after reduction [B3LYP/6-311g(d,p)]; (d) calculated HOMA and NICS(1)$_{zz}$ values for the central ring "A" of **BN-Ph** in different redox states. (e) Constitutional structures of the five different redox states of **BN-Ph**.

DOI: 10.1021/jacs.8b11337
J. Am. Chem. Soc. XXXX, XXX, XXX−XXX

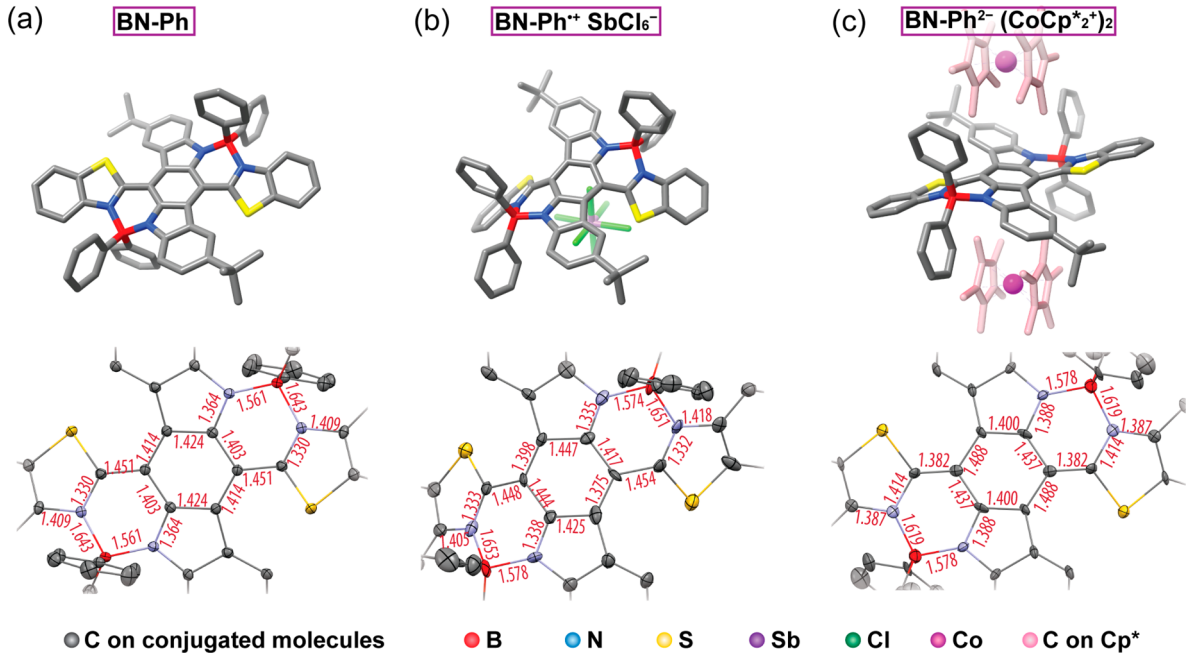

Figure 6. Single-crystal X-ray structures of (a) **BN-Ph**, (b) **BN-Ph**$^{\bullet+}$**SbCl**$_6^-$, and (c) **BN-Ph**$^{2-}$[**CoCp***$_2^+$]$_2$ and bond lengths of the area around the central ring "A". Hydrogen atoms and solvent molecules were omitted for clarity. Thermal ellipsoids are scaled to the 50% probability level.

reduction (Figure 5e), respectively, contributing to the excellent stability in all the oxidized and reduced forms of **BN-Ph**. Considering the noncovalent nature of B ← N coordinate bonds, the molecular geometries were also optimized at the level of B3LYP/TZVP with D3 version of Grimme's dispersion correction, which revealed similar structural transformations (Figure S15). Similar BLA changes and structural transformations were also observed in the optimized molecular geometries for different redox states of **BN-F**. In addition, the aromaticity of ring "A" was calculated using the harmonic oscillator model of aromaticity (HOMA) and the nucleus-independent chemical shift (NICS) values[57−59] (Figure 5d). Both calculations confirmed a strong aromaticity of ring "A" in the neutral state and decreased aromaticity upon oxidation or reduction.

To validate these DFT computational results, the bond lengths and molecular geometries were examined by using experimental data from single-crystal X-ray diffraction of the neutral **BN-Ph**, the radical cation salt **BN-Ph**$^{\bullet+}$**SbCl**$_6^-$, and the dianion salt **BN-Ph**$^{2-}$[**CoCp***$_2^+$]$_2$ (Figure 6). The radical cation was chemically accessed by one-electron oxidation of **BN-Ph** with 1.2 equiv of tris(4-bromophenyl)ammoniumyl hexachloroantimonate (Magic Blue) in a CH_2Cl_2 solution. The single crystals suitable for X-ray diffraction were grown by slow vapor diffusion of pentane into a CH_2Cl_2 solution of **BN-Ph**$^{\bullet+}$**SbCl**$_6^-$. The dianion, on the other hand, was chemically prepared after two-electron reduction of **BN-Ph** by the addition of 3.0 equiv of decamethylcobaltocene (CoCp*$_2$). Vapor diffusion of diethyl ether into a concentrated solution of **BN-Ph**$^{2-}$ in acetonitrile yielded single crystals suitable for X-ray diffraction analysis. Bond lengths measured from the single-crystal structures of **BN-Ph**, **BN-Ph**$^{\bullet+}$**SbCl**$_6^-$, and **BN-Ph**$^{2-}$[**CoCp***$_2^+$]$_2$ matched well (Figure 7) with the DFT calculated bond lengths, further confirming the mechanism of the orthogonal quinonoid transformations upon oxidation and reduction, respectively. The average difference between the bond lengths calculated at the level of B3LYP/6-311g(d,p) and

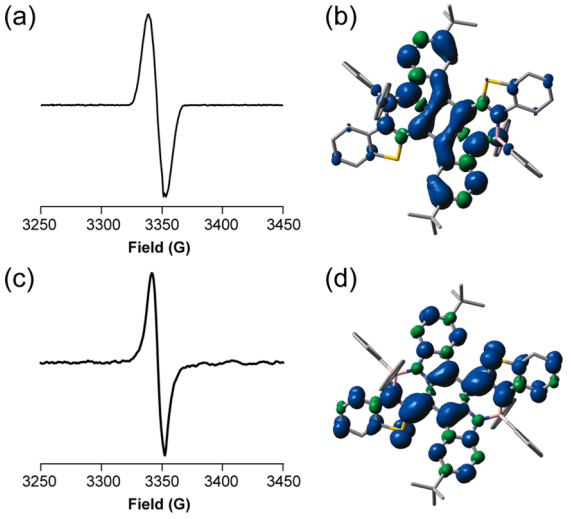

Figure 7. Electron paramagnetic resonance (EPR) spectra of (a) **BN-Ph**$^{\bullet+}$ in CH_2Cl_2 (0.13 mM) and (c) **BN-Ph**$^{\bullet-}$ in acetonitrile (0.03 mM) at 288 K. DFT computed spin density maps (isovalue = 0.0008) of (b) **BN-Ph**$^{\bullet+}$ and (d) **BN-Ph**$^{\bullet-}$ [UB3LYP/6-311g++(d,p)].

experimentally measured bond lengths was only 0.010 Å (see Table S6 for a detailed list). Such an average difference obtained from calculation at the level of B3LYP/TZVP with D3 version of Grimme's dispersion correction was also ~0.010 Å (see Table S7 for a detailed list), suggesting highly reliable computation results. The only exception was bond *d*, which was longer in the neutral state (1.444 Å) from the experimental result than that from the calculation, likely because of the steric strain between ICBZ and BTH units. In both **BN-Ph**$^{\bullet+}$ and **BN-Ph**$^{2-}$, the B ← N coordinate bonds retained their strength so that the rigid backbone scaffolds were maintained. In fact, the B ← N coordinate bond was even shorter in **BN-Ph**$^{2-}$ (1.619 Å) as a result of the stronger Lewis basicity of the nitrogen center on BTH after reduction. Moreover, the

DOI: 10.1021/jacs.8b11337
J. Am. Chem. Soc. XXXX, XXX, XXX−XXX

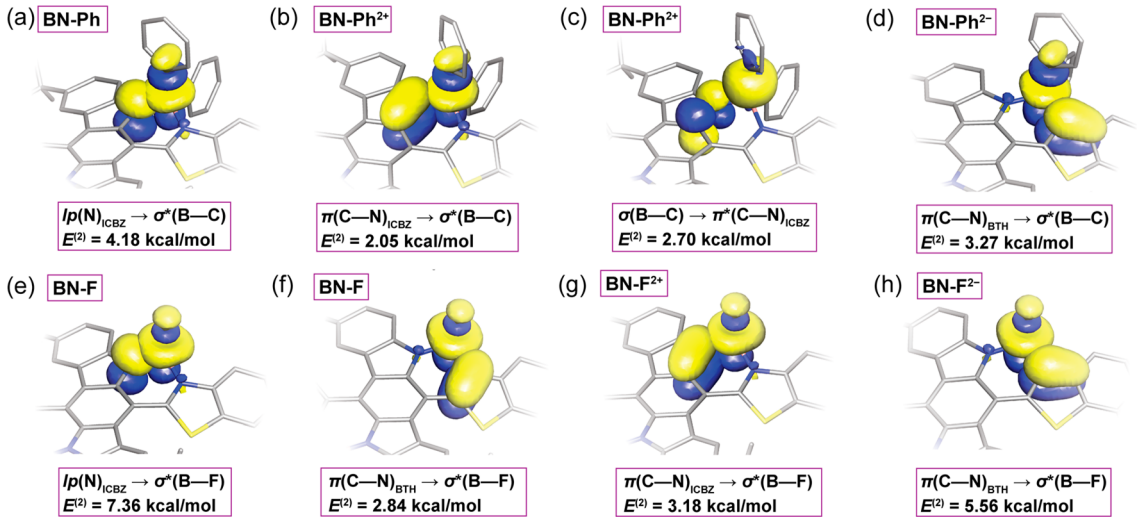

Figure 8. NBO plots of hyperconjugative interactions in different redox states of **BN-Ph** (a, b, c, d) and **BN-F** (e, f, g, h).

backbone of **BN-Ph**$^{2-}$ was more coplanar compared to that of **BN-Ph** (dihedral angles between ICBZ and BTH units reduced to 6.3°), due to an enhanced double-bond character of bonds *j* and *m*.

Additional characterizations were performed on the reduced and oxidized states of **BN-Ph** in order to further understand their electronic structures during the redox processes. Electron paramagnetic resonance (EPR) spectroscopy of the **BN-Ph**$^{\bullet+}$**SbCl**$_6^-$ solution showed a broad resonance signal (Figure 7a). The spin concentration (7.8×10^{17} spin/mL) was close to the theoretical value (8.9×10^{17} spin/mL) when assuming the formation of an organic monoradical ($S = 1/2$) on each molecule, indicative of a high conversion from **BN-Ph** to **BN-Ph**$^{\bullet+}$. The lack of hyperfine splitting in the EPR spectrum was attributed to the delocalized spin that experienced multiple couplings with a number of nuclei in this molecule,[37] in accordance with DFT computed substantial delocalization of the unpaired spin density (Figure 7b and Figure S13).

Overall, experimental investigations together with computational studies clearly revealed the underlying mechanism of the unique redox processes of ladder-type **BN-Ph** molecules, which involved two distinct pathways of constitutional changes from a benzenoid structure into two types of quinonoid structures upon oxidation and reduction, respectively. The oxidation-active moiety and reduction-active moiety were orthogonally compacted into a single molecular scaffold, giving rise to the reversible multistage redox processes. In addition, B ← N coordination promoted the rigid ladder-type structure in which separated redox centers were strongly coupled with each other, and the unpaired electron of radicals was stabilized by extensive delocalization.

In **BN-Ph** and **BN-F**, the boron centers stabilized the redox state through a number of different mechanisms, including spin coupling, extending pi-delocalization, and modulating electron densities. It was also hypothesized that the boron-ligand moieties impacted the electronic structures of these molecules through hyperconjugation similar to that existing in cyclohexa-1,3-diene (Figure 1b), providing additional stabilization effects. According to the crystal structures of **BN-Ph**, **BN-Ph**$^{\bullet+}$, and **BN-Ph**$^{2-}$, the two phenyl ligands on the boron center adopted different bonding orientations: one of the B−C σ-bonds was almost perpendicular to the conjugated backbone (denoted as the "axial" bond), while the other one was almost in the plane of the backbone (denoted as the "equatorial" bond). Such an unsymmetrical geometry of the boron ligand (B—L, L = Ph or F) bonds was also predicted by DFT optimized structures of both **BN-Ph** and **BN-F**. The nonequivalent bonding orientations suggested hyperconjugative interactions between the axial bonds and the conjugated backbone in these ladder-type molecules. To unveil the hyperconjugations of these axial B—L σ/σ^* orbitals, natural bond orbital (NBO) analysis was performed on **BN-Ph**, **BN-F**, and their dianionic and dicationic forms.[48,60] The strengths of these interactions can be correlated with second-order perturbation energies [$E^{(2)}$] computed from NBO analysis.[61,62] In the neutral state of **BN-Ph**, a hyperconjugative donor−acceptor interaction [$E^{(2)}$ = 4.18 kcal/mol] was identified from the lone pair [*lp*(N)] on the ICBZ unit to the antibonding [σ^*(B−C)] orbital on the axial position (Figure 8a).[61] After the two-electron oxidation, the quinonoid ICBZ unit of **BN-Ph**$^{2+}$ lost the lone pair on the nitrogen center and had a lower electron density. Despite a weaker electron-donating ability, the π(C−N) orbital of the quinonoid ICBZ still interacted hyperconjugatively [$E^{(2)}$ = 2.05 kcal/mol] with the axial σ^*(B−C) orbital (Figure 8b). More interestingly, a unique back-donating interaction [$E^{(2)}$ = 2.70 kcal/mol] was observed from the σ(B−C) orbital to the π^*(C−N) orbital of the electron-deficient, quinonoid ICBZ unit (Figure 8c), reinforcing the hyperconjugative stabilization effect by diluting the positive charges on the dicationic backbone of **BN-Ph**$^{2+}$. In the reduced form of dianionic **BN-Ph**$^{2-}$, the NBO analysis showed that the σ^*(B−C) orbital also served as an acceptor to stabilize the negative charges on the reduced BTH units. In **BN-Ph**$^{2-}$, bonds *p* and *q* (Figure 5a) possessed a partial double-bond character (1.387 Å in the crystal structure) so that their π orbitals participated in a hyperconjugation [$E^{(2)}$ = 3.27 kcal/mol] with the σ^*(B−C) orbital (Figure 8d). In this case, the hyperconjugation further delocalized the negative charges and, therefore, enhanced the stability of the highly charged dianion.

In **BN-F** with the fluoride ligands, NBO analysis at different redox states demonstrated similar but even stronger hyperconjugative interactions between the axial σ^*(B−F) orbital and the conjugated backbone, as a result of the high electronegativity of fluorine atoms (Figure 8e−h). In the optimized structure of **BN-F**, the axial σ^*(B−F) orbitals withdrew the electron density through hyperconjugation [$E^{(2)}$ = 7.36 kcal/

DOI: 10.1021/jacs.8b11337
J. Am. Chem. Soc. XXXX, XXX, XXX−XXX

mol] from the electron lone pair of the nitrogen atom on the ICBZ unit (Figure 8e). Meanwhile, another donor−acceptor interaction of 2.84 kcal/mol was found in **BN-F** between the π(C−N) bond in the BTH unit and the axial σ^*(B−F) orbital (Figure 8f). Therefore, these profound hyperconjugative effects in **BN-F**, together with the inductive effect from fluorine atoms, contributed to its low-lying HOMO and LUMO levels compared to **BN-Ph**.

According to DFT calculation, these hyperconjugative interactions were also present in the paramagnetic radical cations and radical anions. Isotropic Fermi couplings of the axial ligands with the already delocalized spin were much higher than those of the equatorial ligands, indicating strong interactions between the axial bond with the backbone through hyperconjugation. Overall, the hyperconjugative stabilization effect further assisted the desirable charge and spin delocalization during the redox processes. Meanwhile, such orbital interactions provided an additional mechanism to impact the electronic structures and properties of the entire ladder-type molecules.

CONCLUSION

In conclusion, we demonstrated herein a molecular design strategy to achieve highly reversible, multistage redox activities and multicolor electrochromism in compact ladder-type molecules bridged with B ← N coordination. The structural transformations from a benzenoid constitution into two distinct types of quinonoid constitutions during both reduction and oxidation processes were elucidated, giving a clear mechanistic picture of these robust multistage electron-transfer processes. Combined theoretical and experimental investigations demonstrated that the B ← N coordination played a pivotal role in rendering the remarkable redox properties of these molecules by extending the charge and spin delocalization and by enforcing the rigid conformation. We systematically established a hyperconjugation mechanism that impacted the electronic structures and further stabilized the different redox states. These results advanced fundamental knowledge of sp^3 boron-containing π-systems, providing practical design principles for the development of *p*-block element-derived molecules and macromolecules with exotic optical, electronic, and spin properties, such as fully fused ladder polymers bridged by these B ← N coordinate bonds.

ASSOCIATED CONTENT

Supporting Information

The Supporting Information is available free of charge on the ACS Publications website at DOI: 10.1021/jacs.8b11337.

General methods, synthesis, characterization data, and computational data (PDF)
Crystallographic data (CIF)
Crystallographic data (CIF)
Crystallographic data (CIF)
DFT calculation optimized structures (XYZ)
DFT calculation optimized structures (DOCX)

AUTHOR INFORMATION

Corresponding Author

*fang@chem.tamu.edu

ORCID

Congzhi Zhu: 0000-0002-1302-7187
Yi Liu: 0000-0002-3954-6102
Lei Fang: 0000-0003-4757-5664

Notes

The authors declare no competing financial interest.

ACKNOWLEDGMENTS

The authors acknowledge National Science Foundation (Award no. 1654029) and the Welch Foundation (A-1898) for financial support of this work. The authors also thank Dr. Oleg V. Ozerov and Cheng-Han Yu for the support of cyclic voltammetry measurement, Dr. Nattamai Bhuvanesh for single-crystal X-ray diffraction measurements, and the Laboratory for Molecular Simulation and High Performance Computing facilities at TAMU for providing software, support, and computer time. Work at the Molecular Foundry was supported by the Office of Science, Office of Basic Energy Sciences, of the U.S. Department of Energy under Contract no. DE-AC02-05CH11231.

REFERENCES

(1) Lee, J.; Kalin, A. J.; Yuan, T.; Al-Hashimi, M.; Fang, L. Fully conjugated ladder polymers. *Chem. Sci.* **2017**, *8*, 2503−2521.
(2) Zou, Y.; Ji, X.; Cai, J.; Yuan, T.; Stanton, D. J.; Lin, Y.-H.; Naraghi, M.; Fang, L. Synthesis and Solution Processing of a Hydrogen-Bonded Ladder Polymer. *Chem.* **2017**, *2*, 139−152.
(3) Cai, Z.; Awais, M. A.; Zhang, N.; Yu, L. Exploration of Syntheses and Functions of Higher Ladder-type π-Conjugated Heteroacenes. *Chem.* **2018**, *4*, 2538−2570.
(4) Wang, Y.; Guo, H.; Ling, S.; Arrechea-Marcos, I.; Wang, Y.; López Navarrete, J. T.; Ortiz, R. P.; Guo, X. Ladder-type Heteroarenes: Up to 15 Rings with Five Imide Groups. *Angew. Chem., Int. Ed.* **2017**, *56*, 9924−9929.
(5) Cai, Z.; Lo, W.-Y.; Zheng, T.; Li, L.; Zhang, N.; Hu, Y.; Yu, L. Exceptional Single-Molecule Transport Properties of Ladder-Type Heteroacene Molecular Wires. *J. Am. Chem. Soc.* **2016**, *138*, 10630−10635.
(6) Cai, Z.; Zhang, N.; Awais, M. A.; Filatov, A. S.; Yu, L. Synthesis of Alternating Donor−Acceptor Ladder-Type Molecules and Investigation of Their Multiple Charge-Transfer Pathways. *Angew. Chem., Int. Ed.* **2018**, *57*, 6442−6448.
(7) Zheng, T.; Cai, Z.; Ho-Wu, R.; Yau, S. H.; Shaparov, V.; Goodson, T.; Yu, L. Synthesis of Ladder-Type Thienoacenes and Their Electronic and Optical Properties. *J. Am. Chem. Soc.* **2016**, *138*, 868−875.
(8) Jin, Z.; Teo, Y. C.; Teat, S. J.; Xia, Y. Regioselective Synthesis of [3]Naphthylenes and Tuning of Their Antiaromaticity. *J. Am. Chem. Soc.* **2017**, *139*, 15933−15939.
(9) Wang, X.-Y.; Lin, H.-R.; Lei, T.; Yang, D.-C.; Zhuang, F.-D.; Wang, J.-Y.; Yuan, S.-C.; Pei, J. Azaborine Compounds for Organic Field-Effect Transistors: Efficient Synthesis, Remarkable Stability, and BN Dipole Interactions. *Angew. Chem.* **2013**, *125*, 3199−3202.
(10) Wang, X.-Y.; Zhuang, F.-D.; Wang, R.-B.; Wang, X.-C.; Cao, X.-Y.; Wang, J.-Y.; Pei, J. A Straightforward Strategy toward Large BN-Embedded π-Systems: Synthesis, Structure, and Optoelectronic Properties of Extended BN Heterosuperbenzenes. *J. Am. Chem. Soc.* **2014**, *136*, 3764−3767.
(11) Stec, G. J.; Lauchner, A.; Cui, Y.; Nordlander, P.; Halas, N. J. Multicolor Electrochromic Devices Based on Molecular Plasmonics. *ACS Nano* **2017**, *11*, 3254−3261.
(12) Wetzel, C.; Brier, E.; Vogt, A.; Mishra, A.; Mena-Osteritz, E.; Bäuerle, P. Fused Thiophene-Pyrrole-Containing Ring Systems up to a Heterodecacene. *Angew. Chem., Int. Ed.* **2015**, *54*, 12334−12338.
(13) Gu, Y.; Wu, X.; Gopalakrishna, T. Y.; Phan, H.; Wu, J. Graphene-like Molecules with Four Zigzag Edges. *Angew. Chem., Int. Ed.* **2018**, *57*, 6541−6545.
(14) Woodward, A. N.; Kolesar, J. M.; Hall, S. R.; Saleh, N.-A.; Jones, D. S.; Walter, M. G. Thiazolothiazole Fluorophores Exhibiting

DOI: 10.1021/jacs.8b11337
J. Am. Chem. Soc. XXXX, XXX, XXX−XXX

Strong Fluorescence and Viologen-Like Reversible Electrochromism. *J. Am. Chem. Soc.* **2017**, *139*, 8467−8473.
(15) Li, G.; Xu, L.; Zhang, W.; Zhou, K.; Ding, Y.; Liu, F.; He, X.; He, G. Narrow-Bandgap Chalcogenoviologens for Electrochromism and Visible-Light-Driven Hydrogen Evolution. *Angew. Chem., Int. Ed.* **2018**, *57*, 4897−4901.
(16) Wakamiya, A.; Taniguchi, T.; Yamaguchi, S. Intramolecular B−N Coordination as a Scaffold for Electron-Transporting Materials: Synthesis and Properties of Boryl-Substituted Thienylthiazoles. *Angew. Chem., Int. Ed.* **2006**, *45*, 3170−3173.
(17) Crossley, D. L.; Cade, I. A.; Clark, E. R.; Escande, A.; Humphries, M. J.; King, S. M.; Vitorica-Yrezabal, I.; Ingleson, M. J.; Turner, M. L. Enhancing electron affinity and tuning band gap in donor−acceptor organic semiconductors by benzothiadiazole directed C−H borylation. *Chem. Sci.* **2015**, *6*, 5144−5151.
(18) Grandl, M.; Sun, Y.; Pammer, F. Generation of an N→B Ladder-type Structure by Regioselective Hydroboration of an Alkenyl-Functionalized Quaterpyridine. *Chem. - Eur. J.* **2016**, *22*, 3976−3980.
(19) Zhu, C.; Guo, Z.-H.; Mu, A. U.; Liu, Y.; Wheeler, S. E.; Fang, L. Low Band Gap Coplanar Conjugated Molecules Featuring Dynamic Intramolecular Lewis Acid−Base Coordination. *J. Org. Chem.* **2016**, *81*, 4347−4352.
(20) Zhu, C.; Fang, L. Locking the Coplanar Conformation of π-Conjugated Molecules and Macromolecules Using Dynamic Non-covalent Bonds. *Macromol. Rapid Commun.* **2018**, *39*, 1700241.
(21) Huang, H.; Yang, L.; Facchetti, A.; Marks, T. J. Organic and Polymeric Semiconductors Enhanced by Noncovalent Conformational Locks. *Chem. Rev.* **2017**, *117*, 10291−10318.
(22) Shimogawa, H.; Yoshikawa, O.; Aramaki, Y.; Murata, M.; Wakamiya, A.; Murata, Y. 4,7-Bis[3-(dimesitylboryl)thien-2-yl]-benzothiadiazole: Solvato-, Thermo-, and Mechanochromism Based on the Reversible Formation of an Intramolecular B−N Bond. *Chem. - Eur. J.* **2017**, *23*, 3784−3791.
(23) Dou, C.; Long, X.; Ding, Z.; Xie, Z.; Liu, J.; Wang, L. An Electron-Deficient Building Block Based on the B ← N Unit: An Electron Acceptor for All-Polymer Solar Cells. *Angew. Chem., Int. Ed.* **2016**, *55*, 1436−1440.
(24) Rao, Y.-L.; Amarne, H.; Zhao, S.-B.; McCormick, T. M.; Martić, S.; Sun, Y.; Wang, R.-Y.; Wang, S. Reversible Intramolecular C−C Bond Formation/Breaking and Color Switching Mediated by a N,C-Chelate in (2-ph-py)BMes2 and (5-BMes2−2-ph-py)BMes2. *J. Am. Chem. Soc.* **2008**, *130*, 12898−12900.
(25) Liu, K.; Lalancette, R. A.; Jäkle, F. B−N Lewis Pair Functionalization of Anthracene: Structural Dynamics, Optoelectronic Properties, and O2 Sensitization. *J. Am. Chem. Soc.* **2017**, *139*, 18170−18173.
(26) Yusuf, M.; Liu, K.; Guo, F.; Lalancette, R. A.; Jäkle, F. Luminescent organoboron ladder compounds via directed electrophilic aromatic C−H borylation. *Dalton Trans.* **2016**, *45*, 4580−4587.
(27) Wakamiya, A.; Murakami, T.; Yamaguchi, S. Benzene-fused BODIPY and fully-fused BODIPY dimer: impacts of the ring-fusing at the b bond in the BODIPY skeleton. *Chem. Sci.* **2013**, *4*, 1002−1007.
(28) Alahmadi, A. F.; Lalancette, R. A.; Jäkle, F. Highly Luminescent Ladderized Fluorene Copolymers Based on B−N Lewis Pair Functionalization. *Macromol. Rapid Commun.* **2018**, *39*, 1800456.
(29) Dou, C.; Liu, J.; Wang, L. Conjugated polymers containing B←N unit as electron acceptors for all-polymer solar cells. *Sci. China: Chem.* **2017**, *60*, 450−459.
(30) Qiu, F.; Zhang, F.; Tang, R.; Fu, Y.; Wang, X.; Han, S.; Zhuang, X.; Feng, X. Triple Boron-Cored Chromophores Bearing Discotic 5,11,17-Triazatrinaphthylene-Based Ligands. *Org. Lett.* **2016**, *18*, 1398−1401.
(31) Wang, X.-Y.; Narita, A.; Feng, X.; Müllen, K. B2N2-Dibenzo[a,e]pentalenes: Effect of the BN Orientation Pattern on Antiaromaticity and Optoelectronic Properties. *J. Am. Chem. Soc.* **2015**, *137*, 7668−7671.
(32) Wang, X.-Y.; Wang, J.-Y.; Pei, J. BN Heterosuperbenzenes: Synthesis and Properties. *Chem. - Eur. J.* **2015**, *21*, 3528−3539.
(33) Hou, Q.; Liu, L.; Mellerup, S. K.; Wang, N.; Peng, T.; Chen, P.; Wang, S. Stimuli-Responsive B/N Lewis Pairs Based on the Modulation of B−N Bond Strength. *Org. Lett.* **2018**, *20*, 6467−6470.
(34) Yang, D.-T.; Mellerup, S. K.; Peng, J.-B.; Wang, X.; Li, Q.-S.; Wang, S. Substituent Directed Phototransformations of BN-Heterocycles: Elimination vs Isomerization via Selective B−C Bond Cleavage. *J. Am. Chem. Soc.* **2016**, *138*, 11513−11516.
(35) Grandl, M.; Rudolf, B.; Sun, Y.; Bechtel, D. F.; Pierik, A. J.; Pammer, F. Intramolecular N → B Coordination as a Stabilizing Scaffold for π -Conjugated Radical Anions with Tunable Redox Potentials. *Organometallics* **2017**, *36*, 2527−2535.
(36) Su, Y.; Kinjo, R. Boron-containing radical species. *Coord. Chem. Rev.* **2017**, *352*, 346−378.
(37) Ji, L.; Edkins, R. M.; Lorbach, A.; Krummenacher, I.; Brückner, C.; Eichhorn, A.; Braunschweig, H.; Engels, B.; Low, P. J.; Marder, T. B. Electron Delocalization in Reduced Forms of 2-(BMes2)pyrene and 2,7-Bis(BMes2)pyrene. *J. Am. Chem. Soc.* **2015**, *137*, 6750−6753.
(38) Ji, L.; Griesbeck, S.; Marder, T. B. Recent developments in and perspectives on three-coordinate boron materials: a bright future. *Chem. Sci.* **2017**, *8*, 846−863.
(39) Luo, D.; Lee, S.; Zheng, B.; Sun, Z.; Zeng, W.; Huang, K.-W.; Furukawa, K.; Kim, D.; Webster, R. D.; Wu, J. Indolo[2,3-b]carbazoles with tunable ground states: how Clar's aromatic sextet determines the singlet biradical character. *Chem. Sci.* **2014**, *5*, 4944−4952.
(40) Janosik, T.; Rannug, A.; Rannug, U.; Wahlström, N.; Slätt, J.; Bergman, J. Chemistry and Properties of Indolocarbazoles. *Chem. Rev.* **2018**, *118*, 9058−9128.
(41) Maeda, C.; Todaka, T.; Ueda, T.; Ema, T. Synthesis of carbazole-based BODIPY dimers showing red fluorescence in the solid state. *Org. Biomol. Chem.* **2017**, *15*, 9283−9287.
(42) Maeda, C.; Nagahata, K.; Ema, T. Carbazole-based BODIPYs with ethynyl substituents at the boron center: solid-state excimer fluorescence in the VIS/NIR region. *Org. Biomol. Chem.* **2017**, *15*, 7783−7788.
(43) Curiel, D.; Más-Montoya, M.; Usea, L.; Espinosa, A.; Orenes, R. A.; Molina, P. Indolocarbazole-Based Ligands for Ladder-Type Four-Coordinate Boron Complexes. *Org. Lett.* **2012**, *14*, 3360−3363.
(44) Knowles, C. M.; Watt, G. W. The Reduction of Benzoxazoles and Benzothiazoles in Liquid Ammonia. *J. Org. Chem.* **1942**, *07*, 56−62.
(45) Ulrich, G.; Ziessel, R.; Harriman, A. The Chemistry of Fluorescent Bodipy Dyes: Versatility Unsurpassed. *Angew. Chem., Int. Ed.* **2008**, *47*, 1184−1201.
(46) Loudet, A.; Burgess, K. BODIPY Dyes and Their Derivatives: Syntheses and Spectroscopic Properties. *Chem. Rev.* **2007**, *107*, 4891−4932.
(47) Mehta, G.; Uma, R. Stereoelectronic Control in Diels−Alder Reaction of Dissymmetric 1,3-Dienes. *Acc. Chem. Res.* **2000**, *33*, 278−286.
(48) Alabugin, I. V.; Gilmore, K. M.; Peterson, P. W. Hyperconjugation. *Wiley Interdiscip. Rev. Comput. Mol. Sci.* **2011**, *1*, 109−141.
(49) Ajayakumar, M. R.; Asthana, D.; Mukhopadhyay, P. Core-Modified Naphthalenediimides Generate Persistent Radical Anion and Cation: New Panchromatic NIR Probes. *Org. Lett.* **2012**, *14*, 4822−4825.
(50) Yao, C.-J.; Zhong, Y.-W.; Nie, H.-J.; Abruña, H. D.; Yao, J. Near-IR Electrochromism in Electropolymerized Films of a Biscyclometalated Ruthenium Complex Bridged by 1,2,4,5-Tetra(2-pyridyl)benzene. *J. Am. Chem. Soc.* **2011**, *133*, 20720−20723.
(51) Dyer, A. L.; Grenier, C. R. G.; Reynolds, J. R. A Poly(3,4-alkylenedioxythiophene) Electrochromic Variable Optical Attenuator with Near-Infrared Reflectivity Tuned Independently of the Visible Region. *Adv. Funct. Mater.* **2007**, *17*, 1480−1486.
(52) Mortimer, R. J. Electrochromic Materials. *Annu. Rev. Mater. Res.* **2011**, *41*, 241−268.

DOI: 10.1021/jacs.8b11337
J. Am. Chem. Soc. XXXX, XXX, XXX−XXX

(53) Mee, S. P. H.; Lee, V.; Baldwin, J. E. Stille Coupling Made Easier—The Synergic Effect of Copper(I) Salts and the Fluoride Ion. *Angew. Chem., Int. Ed.* **2004**, *43*, 1132−1136.
(54) Jiang, W.; Tang, J.; Ban, X.; Sun, Y.; Duan, L.; Qiu, Y. Ideal Bipolar Host Materials with Bis-benzimidazole Unit for Highly Efficient Solution-Processed Green Electrophosphorescent Devices. *Org. Lett.* **2014**, *16*, 5346−5349.
(55) Hankache, J.; Wenger, O. S. Organic Mixed Valence. *Chem. Rev.* **2011**, *111*, 5138−5178.
(56) Hansmann, M. M.; Melaimi, M.; Bertrand, G. Organic Mixed Valence Compounds Derived from Cyclic (Alkyl)(amino)carbenes. *J. Am. Chem. Soc.* **2018**, *140*, 2206−2213.
(57) Krygowski, T. M.; Cyrański, M. K. Structural Aspects of Aromaticity. *Chem. Rev.* **2001**, *101*, 1385−1420.
(58) Ke, X.-S.; Hong, Y.; Lynch, V. M.; Kim, D.; Sessler, J. L. Metal-Stabilized Quinoidal Dibenzo[g,p]chrysene-Fused Bis-dicarbacorrole System. *J. Am. Chem. Soc.* **2018**, *140*, 7579−7586.
(59) Lu, T.; Chen, F. Multiwfn: A multifunctional wavefunction analyzer. *J. Comput. Chem.* **2012**, *33*, 580−592.
(60) Tomoda, S.; Senju, T. Natural bond orbital analysis of hyperconjugative stabilization effects in the transition states of cyclohexanone reduction with LiAlH4. *Chem. Commun.* **1999**, 423−424.
(61) Kwon, O.; Sevin, F.; McKee, M. L. Density Functional Calculations of Methyllithium, t-Butyllithium, and Phenyllithium Oligomers: Effect of Hyperconjugation on Conformation. *J. Phys. Chem. A* **2001**, *105*, 913−922.
(62) Alam Sk, M.; Xi, H.-W.; Lim, K. H. Structure, Bonding, and Hyperconjugation of Germaallene: A Theoretical Study. *Organometallics* **2009**, *28*, 3678−3685.

DOI: 10.1021/jacs.8b11337
J. Am. Chem. Soc. XXXX, XXX, XXX−XXX